Direct gap $Ge_{1-y}Sn_y$ alloys: Fabrication and design of mid-IR photodiodes

C. L. Senaratne, P. M. Wallace, J. D. Gallagher, P. E. Sims, J. Kouvetakis, and J. Menéndez

Citation: Journal of Applied Physics **120**, 025701 (2016); doi: 10.1063/1.4956439
View online: http://dx.doi.org/10.1063/1.4956439
View Table of Contents: http://aip.scitation.org/toc/jap/120/2
Published by the American Institute of Physics

Direct gap $Ge_{1-y}Sn_y$ alloys: Fabrication and design of mid-IR photodiodes

C. L. Senaratne,[1] P. M. Wallace,[1] J. D. Gallagher,[2] P. E. Sims,[1] J. Kouvetakis,[1] and J. Menéndez[2]
[1]*School of Molecular Sciences, Arizona State University, Tempe, Arizona 85287-1604, USA*
[2]*Department of Physics, Arizona State University, Tempe, Arizona 85287-1504, USA*

(Received 30 April 2016; accepted 27 June 2016; published online 13 July 2016)

Chemical vapor deposition methods were developed, using stoichiometric reactions of specialty Ge_3H_8 and SnD_4 hydrides, to fabricate $Ge_{1-y}Sn_y$ photodiodes with very high Sn concentrations in the 12%–16% range. A unique aspect of this approach is the compatible reactivity of the compounds at ultra-low temperatures, allowing efficient control and systematic tuning of the alloy composition beyond the direct gap threshold. This crucial property allows the formation of thick supersaturated layers with device-quality material properties. Diodes with composition up to 14% Sn were initially produced on Ge-buffered Si(100) featuring previously optimized *n*-Ge/*i*-$Ge_{1-y}Sn_y$/*p*-$Ge_{1-z}Sn_z$ type structures with a single defected interface. The devices exhibited sizable electroluminescence and good rectifying behavior as evidenced by the low dark currents in the I-V measurements. The formation of working diodes with higher Sn content up to 16% Sn was implemented by using more advanced *n*-$Ge_{1-x}Sn_x$/*i*-$Ge_{1-y}Sn_y$/*p*-$Ge_{1-z}Sn_z$ architectures incorporating $Ge_{1-x}Sn_x$ intermediate layers ($x \sim 12\%$ Sn) that served to mitigate the lattice mismatch with the Ge platform. This yielded fully coherent diode interfaces devoid of strain relaxation defects. The electrical measurements in this case revealed a sharp increase in reverse-bias dark currents by almost two orders of magnitude, in spite of the comparable crystallinity of the active layers. This observation is attributed to the enhancement of band-to-band tunneling when all the diode layers consist of direct gap materials and thus has implications for the design of light emitting diodes and lasers operating at desirable mid-IR wavelengths. Possible ways to engineer these diode characteristics and improve carrier confinement involve the incorporation of new barrier materials, in particular, ternary $Ge_{1-x-y}Si_xSn_y$ alloys. The possibility of achieving type-I structures using binary and ternary alloy combinations is discussed in detail, taking into account the latest experimental and theoretical work on band offsets involving such materials. *Published by AIP Publishing.*
[http://dx.doi.org/10.1063/1.4956439]

I. INTRODUCTION

Substantial progress has been made in the development of $Ge_{1-y}Sn_y$ alloys since the introduction of a viable Chemical Vapor Deposition (CVD) route in 2002.[1] This progress is remarkable if one considers that the room-temperature solid solubility of Sn in Ge is less than 1%.[2,3] In spite of this thermodynamic constraint, however, device-quality alloys with very high metastable Sn concentrations are now routinely synthesized.[4–6] These metastable alloys are not simple academic curiosities but have been incorporated into real device structures, including optically pumped lasers with compositions reaching 13% Sn,[7] and electroluminescent diodes with Sn concentrations above 10%.[8]

While the most recent generation of devices exceed the indirect-to-direct transition concentration $y_c \sim 9\%$ Sn,[9] fulfilling one of the basic goals of $Ge_{1-y}Sn_y$ research, there are fundamental and practical reasons for pursuing the development of $Ge_{1-y}Sn_y$ alloys with Sn concentrations well in excess of y_c. Near y_c, carriers pumped into the conduction band at room temperature reside mainly in the indirect L valleys—even in formally direct-gap materials—due to the very large density of states difference between the L minima and the direct valley at the Γ-point of the Brillouin zone (BZ). We estimate that for 5×10^{17} cm^{-3} excited carriers in the conduction band, the population of the direct valley only reaches 50% of the pumped carriers for a Sn concentration $y = 21\%$. Another potentially important consideration is illustrated in Fig. 1. Auger recombination has been identified by Sun and coworkers[10] as the main factor preventing $Ge_{1-y}Sn_y$ lasers from operating at room temperature. But as the Sn concentration is increased, the spin-orbit splitting Δ_0 increases and the direct gap E_0 decreases, which reduces and eventually eliminates

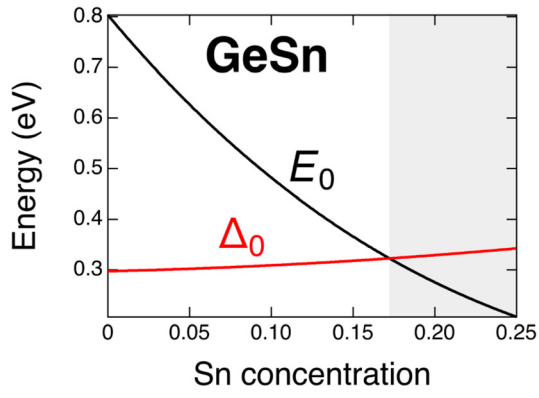

FIG. 1. Comparison of the direct band gap E_0 and the spin-orbit splitting Δ_0 in $Ge_{1-y}Sn_y$ alloys. The shaded area corresponds to concentrations for which Auger recombination is suppressed.

(for $E_0 < \Delta_0$) Auger recombination involving hot holes, the dominant loss contribution in near infrared (NIR) lasers.[11] From Fig. 1, the required concentration to achieve this condition is $y_A \sim 17\%$. At even higher Sn concentrations approaching the semiconductor-semimetal threshold, $Ge_{1-y}Sn_y$ alloys may represent a viable alternative to $Hg_{1-x}Cd_xTe$ alloys for far-IR applications integrated on Si platforms.

The far infrared potential of $Ge_{1-y}Sn_y$ alloys requires an extension of the metastability window to much higher Sn concentrations than currently achieved. In this paper, we demonstrate that the CVD approach based on the Ge_3H_8/SnD_4 precursors can be extended to at least $y = 16\%$ by fabricating and testing a series of *pin* diodes containing such alloys. The use of real devices as a benchmark is important because, in addition to avoiding catastrophic segregation into distinct phases, the high-Sn material must remain free of crystalline defects that limit device performance. Some of these possible defects, such as the so-called β-Sn inclusion—in which a Sn atom fills a double vacancy in the Ge lattice—are predicted to become more abundant as the Sn concentration grows, and might preclude the use of high-Sn $Ge_{1-y}Sn_y$ in practical devices even if the material does not decompose.[12] We find that strain management at the interface between the high-Sn $Ge_{1-y}Sn_y$ film and the buffer layer remains the major consideration for achieving high-quality growth. No obvious synthetic barriers are identified in our experiments, suggesting that further increases the Sn concentration in practical device structures may be possible. The remainder of the paper is organized as follows: in Section II, we critically discuss the possible synthetic paths to high-Sn materials and justify our choice of the Ge_3H_8/SnD_4 route. In Section III, we present our results for devices grown on Ge-buffer layers, with which we demonstrate Sn concentrations reaching 14%. In Section IV, we show that even higher Sn concentrations can be achieved by inserting intermediate-composition $Ge_{1-x}Sn_x$ layers that mitigate the lattice mismatch between Ge and $Ge_{1-y}Sn_y$. Finally, some prospectives for further progress are discussed in Section V.

II. SYNTHETIC APPROACH

Two distinct CVD approaches have emerged in the quest for high-Sn $Ge_{1-y}Sn_y$ alloys. The first method, introduced by our group, uses the inorganic Sn precursor deuterostannane (SnD_4) as the Sn source. An alternative route is based on $SnCl_4$,[13,14] which has the advantage of being favored in certain industrial tools. The SnD_4 precursor was initially demonstrated in combination with digermane (Ge_2H_6),[1] but subsequent work has shown that trigermane (Ge_3H_8) is ideally compatible with SnD_4,[15] leading to a nearly equal incorporation efficiency for Ge and Sn. This makes it very simple to control the film composition by varying the precursor gaseous mixture. While stannane SnH_4 is unstable, deuteration increases stability to the point that epitaxy applications become feasible. Long-term storage of SnD_4 for commercial applications has also been demonstrated.[16] The chemistry and applications of group-IV hydrocarbon analogues have been recently reviewed by Rivard.[17]

The alternative $SnCl_4$ precursor is used in combination with Ge_2H_6 as the Ge source.[13,14] In a typical growth experiment, the gas ratio is held constant, and the film compositions are varied by changing the growth temperature[18] while keeping a fixed excess of Ge_2H_6 relative to $SnCl_4$, which in the case of Ref. 18 was as high as $pGe_2H_6/pSnCl_4 = 220$. This indicates that the reactivities of the two precursors are not compatible, leading to a minimal conversion of the Ge_2H_6 starting material to solid product, which makes the process inefficient and costly. We speculate that the large Ge_2H_6 excess used in this process enhances the reactivity of $SnCl_4$ at the low temperatures needed for the substitutional incorporation of Sn. From a reaction mechanism perspective, it is possible that an intermediate step during depositions produces transient SnH_mCl_{4-m} species ($m = 1$–4), which are dramatically less stable than $SnCl_4$ and are therefore better Sn delivery sources.

It is known that $SnCl_4$ acts as a chlorinating agent of Ge_2H_6 when the two molecules are combined in a closed system,[19] readily producing Ge_2H_5Cl and $SnHCl_3$. The latter is highly unstable and eliminates HCl at room temperature, as demonstrated in control experiments conducted in our labs. This indicates that a ligand exchange pathway is favored in direct reactions of Ge_2H_6 and $SnCl_4$ molecules under equilibrium conditions. While CVD is a non-equilibrium process due to the dynamic removal of the reaction components, the large $Ge_2H_6/SnCl_4$ ratio employed in the $SnCl_4$ process may generate a pseudo-equilibrium environment that favors the formation of the unstable SnH_mCl_{4-m} intermediates. The rate of formation may be further increased under the 60 mbar reaction pressure employed in the CVD work of von den Driesch *et al.*, thereby explaining the ability of $SnCl_4$ to deposit Sn at low temperatures despite the relatively high strength of the Sn-Cl bond (0.33 eV).[6,18] A possible mechanism leading to Sn incorporation under these circumstances would involve the following reactions:

$$Ge_2H_6 + SnCl_4 \Rightarrow Ge_2H_5Cl + SnHCl_3, \quad (1)$$

$$Ge_2H_6 + SnHCl_3 \Rightarrow Ge_2H_5Cl + SnH_2Cl_2, \quad (2)$$

$$SnH_2Cl_2 \Rightarrow 2HCl + Sn\,(\text{atoms}). \quad (3)$$

In contrast, in the SnD_4/Ge_3H_8 approach, the requirement of excess Ge precursor is eliminated, which leads to a significant decrease in process cost and eliminates waste of expensive Ge, which is considered a rare element with limited global supply.[20] Furthermore, the decoupling of growth temperature and Sn concentration under this method implies that the growth temperature can be freely adjusted to maximize crystal quality and is not constrained by stoichiometry requirements. The composition control obtained by tuning precursor ratios rather than temperature may also represent a more suitable method for fabricating devices with more complex layer structures that require precise tuning of band gap vs composition. For these reasons, we believe that the SnD_4/Ge_3H_8 system is a more promising route to high-Sn $Ge_{1-y}Sn_y$ alloys, and the work presented here is based on this approach.

III. GROWTH OF n-Ge/i-$Ge_{1-y}Sn_y$/p-$Ge_{1-z}Sn_z$ DIODES

The initial appeal of the CVD approach to $Ge_{1-y}Sn_y$ films was the finding that the films grow directly on Si substrates with nearly complete strain relaxation. However,

subsequent research showed that at the lower temperatures required to achieve Sn concentrations $y > 5\%$, the films are prevented from fully relaxing the mismatch strain with the Si lattice. This, combined with the reduced growth rates, limits the overall thickness that can be achieved, ultimately diminishing the device potential of these materials on Si. A solution of this problem is the insertion of pure Ge buffer layers, which drastically reduce the starting lattice mismatch between the Si(100) substrate and the film.[21] This means that strain relaxation can be achieved with a much lower dislocation density, which facilitates the growth of thick films and reduces the non-radiative recombination velocities at the film-buffer interface. A number of groups have utilized this approach to fabricate *n*-Ge/*i*-$Ge_{1-y}Sn_y$/*p*-Ge heterostructure light emitting diodes (LEDs) in which the GeSn active layers are ensconced by *p*- and *n*-type Ge electrodes.[4,5,22–25] A drawback of such designs, however, is the formation of two defected $Ge_{1-y}Sn_y$/Ge interfaces that act as carrier recombination sites, adversely affecting the emission efficiency of the devices. Our previous work in this area was focused on the fabrication of enhanced performance LEDs by adopting improved *n*-Ge/*i*-$Ge_{1-y}Sn_y$/*p*-$Ge_{1-z}Sn_z$ designs containing a single defected interface. In this case, we were able to achieve significantly stronger light emission from active $Ge_{1-y}Sn_y$ layers with compositions up to $y = 0.11$.[8] Here, we extend this approach to demonstrate *n*-Ge/*i*-$Ge_{1-y}Sn_y$/*p*-$Ge_{1-z}Sn_z$ structures with $y \sim 12\%–14\%$.

The samples produced in this study were grown on Ge-buffered Si substrates. These buffers were deposited directly on 4 in. Si(100) wafers with a thickness of $\sim 1\ \mu m$ using the Ge_4H_{10} precursor. They were doped *in situ* by adding 2% $P(GeH_3)_3$ in relation to the amount of Ge_4H_{10} in the reaction mixture, yielding active donor concentrations of $2 \times 10^{19}\ cm^{-3}$.[26] The intrinsic $Ge_{1-y}Sn_y$ layers were grown upon quadrants cleaved from the doped Ge-buffered Si(100) wafers. Prior to growth, the samples were cleaned by dipping in an aqueous HF bath and then loaded into the ultra-high vacuum chemical vapor deposition (UHV-CVD) reactor under a flow of H_2 at a background pressure of 0.2 Torr. We found that the growth surface quality can be drastically improved by depositing a very thin pure Ge seed layer before starting the alloy growth. This layer was deposited on the doped Ge-buffered Si(100) wafer surface at 340 °C using Ge_3H_8/H_2 mixtures 1.5% by volume. We obtained ~ 100 nm thick seed layers, which provide a clean and uniform template that allows optimal epitaxy of subsequent intrinsic layers of $Ge_{1-y}Sn_y$ alloys. As indicated above, these were grown using gas mixtures containing appropriate concentrations of Ge_3H_8 and SnD_4. The compounds were combined in a 3-L ampule and diluted with research-grade H_2 to a final pressure of 760 Torr. In a typical run, the Ge_3H_8 partial pressure in the mixture was kept constant at 9 Torr, while that of SnD_4 was varied from 2.9 to 3.5 Torr, yielding 0.107–0.126 Sn atoms relative to Ge atoms in the gas phase. These formulations produced alloys with Sn contents ranging from 12% to 13.7%, respectively, indicating that the Ge and Sn content in the films closely reflects the mole fraction of the gaseous mixtures. As such, it can be seen that the amount of Sn incorporated in the epilayer during growth is nearly stoichiometric. The composition control afforded in this case is facilitated by the similar reactivity of the co-reactants, yielding samples with well-defined and reproducible stoichiometries.

The fabrication of $Ge_{1-y}Sn_y$ layers with $y = 0.12–0.137$ was initiated at temperatures ranging from 280 °C to 270 °C, respectively. The growth was allowed to proceed for a sufficient time to produce nucleation layers of the target material at low temperatures, in order to ensure substitutional incorporation of the entire Sn content. After this initial step, the temperature was raised slowly by 5 °C–10 °C and kept constant for the remainder of the experiment. The slight increase facilitated further strain relaxation in the growing layers, generating a more facile template upon which further growth can proceed at a faster rate. By following this procedure, it was possible to obtain uniform films in the target composition with thicknesses up to 430 nm. Due to the large final thickness, high degrees of strain relaxation were observed in all cases, a factor which promotes direct gap behavior. Finally, the device structures were completed by the growth of a top contact layer consisting of a $Ge_{1-z}Sn_z$ alloy which was doped *in-situ* using B_2H_6. The $Ge_{1-z}Sn_z$ *p*-layers of the representative devices discussed here had lower Sn contents of 6%, 10%, and 8% than the corresponding 12%, 12.8%, 13.7% Sn of the active layers. This composition choice was made to increase carrier confinement in the active layer and to minimize reabsorption of the emitted light, while promoting pseudomorphic growth between the two materials in a given device.

The fabricated diode stacks were characterized using Rutherford backscattering (RBS), high resolution X-ray diffraction (HRXRD), spectroscopic ellipsometry, and cross sectional transmission electron microscopy (XTEM). The diodes were found to bear many features in common with similar devices reported earlier spanning Sn compositions from $y = 0.05$ to 0.11.[8,27] The abovementioned Sn contents were determined by RBS. Similar RBS channeling values for Ge and Sn indicate that the Sn is incorporated substitutionally. The active $Ge_{1-y}Sn_y$ layer is mostly relaxed relative to the Ge buffer, and the strain misfit is accommodated by the formation of defects confined to the *n*-Ge/*i*-$Ge_{1-y}Sn_y$ interface. The top *i*-$Ge_{1-y}Sn_y$/*p*-$Ge_{1-z}Sn_z$ interface is fully strained and defect-free due to the absence of strain induced defects, as evidenced by cross sectional scanning transmission electron microscopy (XSTEM) and HRXRD studies. Figure 2 shows representative XSTEM micrographs from a sample comprising a *n*-Ge/*i*-$Ge_{0.863}Sn_{0.137}$/*p*-$Ge_{0.92}Sn_{0.08}$ device stack. Figure 2(a) is a medium angle annular dark field (MAADF) image of the entire device. The intensity contrast in the image is sensitive to both atomic mass (Z-contrast) and strain, and therefore clearly delineates the active and passive layers due to their composition and strain differences. The layers are flat, and the intrinsic and *p*-type components exhibit thicknesses $\sim$ of 340 and 140 nm, respectively. Furthermore, the uniform contrast within the layers indicates homogenous compositions throughout. This observation also provides further evidence that the slight temperature ramp employed during growth of the active layer did not lead to any compositional variations. Figure 2(b) is a high resolution

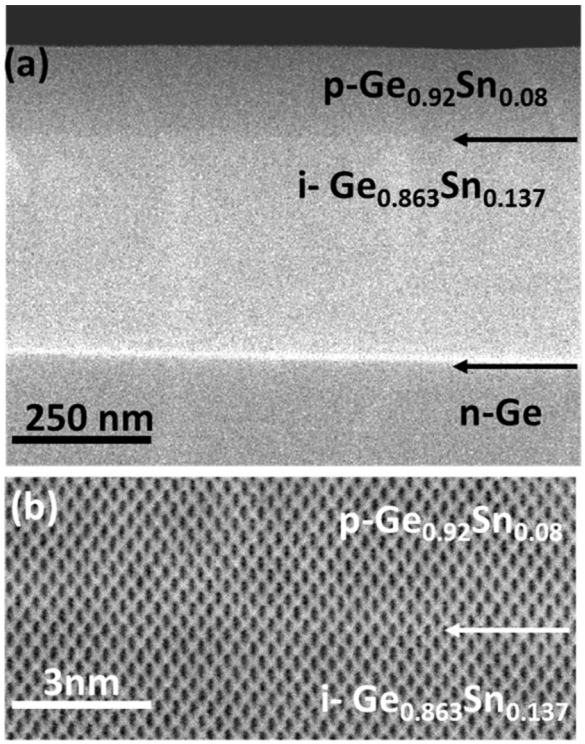

FIG. 2. (a) XSTEM MAADF image of a *pin* device comprising a *n*-Ge bottom contact, *i*-$Ge_{0.863}Sn_{0.137}$ active layer, and *p*-$Ge_{0.92}Sn_{0.08}$ top electrode. The dark and light contrast in the image is consistent with different Sn contents in the layers. The uniform contrast within each layer indicates compositional homogeneity. (b) High resolution image of the *p*-GeSn/*i*-GeSn interface showing no defects due to pseudomorphic growth.

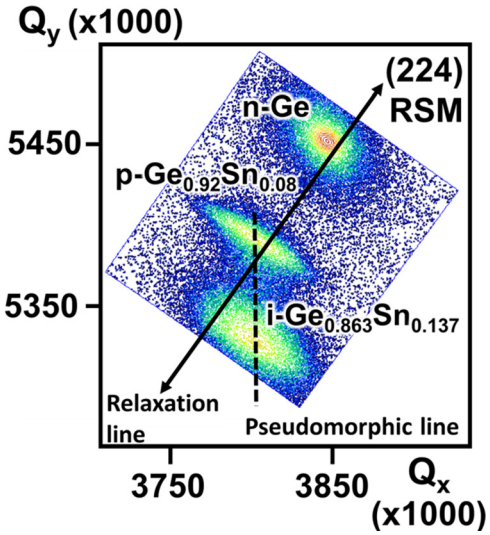

FIG. 3. (224) reciprocal space maps of a *n*-Ge/*i*-$Ge_{0.863}Sn_{0.137}$/*p*-$Ge_{0.92}Sn_{0.08}$ diode. The *p* and *i* layers are nearly lattice matched in the plane of growth as evidenced by the vertical alignment of the peaks, indicated by the dashed pseudomorphic line in the figure.

bright field (BF) image of the top interface showing a defect-free microstructure due to the in plane lattice matching of the *i*-*p* layers. The bottom *n*-*i* interface (not shown) contains 60° dislocations and short stacking faults penetrating down a short distance into the Ge buffer layer, as expected due to the relaxation of the *i*-layer. Figure 3 shows (224) reciprocal space maps of the same sample featuring the various peaks of the device layers and the buffer. The position of the *i*-layer peak is slightly below the relaxation line, indicating the presence of a residual compressive strain. The resultant in-plane and out-of-plane lattice parameters of the $Ge_{0.863}Sn_{0.137}$ alloy are measured to be $a = 5.7304$ Å and $c = 5.7836$ Å, respectively. These are used to derive (via standard elasticity theory[28]) a relaxed cubic cell constant $a_0 = 5.761$ Å, which implies that the strain relaxation reaches 70%. Using the lattice parameter–composition relationship $a_0(y)$ given in Reference 28, we find that the Sn concentrations are the same as determined directly from RBS. The adherence of our samples to the universal $a_0(y)$ curve is consistent with the substitutional nature of the Sn contents. In contrast to the *n*/*i* interface, the XRD maps show that the top *p*-layer is fully strained to the *i*-layer, as evidenced by the vertical alignment of their 224 peaks. This is consistent with the dearth of interface defects in Fig. 2(b). Fortuitously, the *p* layer is nearly cubic with a = 5.728 Å and c = 5.717 Å as seen by the relaxation line passing near the center of the XRD peak. Finally, we note that the analogous devices *n*-Ge/*i*-$Ge_{0.88}Sn_{0.12}$/*p*-$Ge_{0.94}Sn_{0.06}$ and *n*-Ge/*i*-$Ge_{0.872}Sn_{0.128}$/*p*-$Ge_{0.90}Sn_{0.10}$ fabricated in this study also contain a single defected interface between the Ge buffer and the intrinsic $Ge_{0.88}Sn_{0.12}$ and *i*-$Ge_{0.872}Sn_{0.128}$ layers. The latter exhibit large thicknesses of 360 nm and 430 nm, respectively, and are found to be ~70% relaxed while the corresponding *p*-type counterparts $Ge_{0.94}Sn_{0.06}$ (270 nm) and $Ge_{0.90}Sn_{0.10}$ (150 nm) are fully strained and lattice matched. This is likely a result of the ultralow temperature of 275–290 °C employed in the deposition of the *p*-type materials in this case.

The top panel in Fig. 4 shows the I-V curves of the devices demonstrating good rectifying behavior in all cases. The dark currents are relatively low in the range of 7–10 $\times 10^{-1}$ A cm^{-2} and seem to have similar magnitudes to those measured from samples with Sn contents between 8% and 11%, indicating reasonable performance characteristics for the highly concentrated alloys. The diodes were then used to excite electroluminescence. A typical spectrum from the 12% Sn sample is plotted in Figure 4 (b) and compared with that of a 10.5% Sn device from Ref. 8. The plots in both samples were recorded using a thermoelectrically cooled PbS detector, which is the reason for the relatively poor signal-to-noise ratio seen in the plots. By fitting the experimental data with exponentially modified Gaussian (EMG) functions as described in Ref. 29, the peak position for the 12% Sn device was determined to be at 0.47 eV (2640 nm), in good agreement with band gap-composition relationships derived for $Ge_{1-y}Sn_y$ alloys in previous studies.[9] Furthermore, the higher intensity observed for the 12% Sn spectrum is consistent with the expectation that the alloy becomes more direct with increasing Sn content. We note that the emission wavelength of the 12.8% and 13.7% Sn samples is beyond the 2700 nm cutoff of our detector, and thus could not be measured in this study. Nevertheless, the relatively low dark currents of the samples, compared to the 12% analog suggest that the optical quality should be comparable. In this connection, we note that the onset of the EL peak for 12.8% sample was detected indicating that the device should perform as expected.

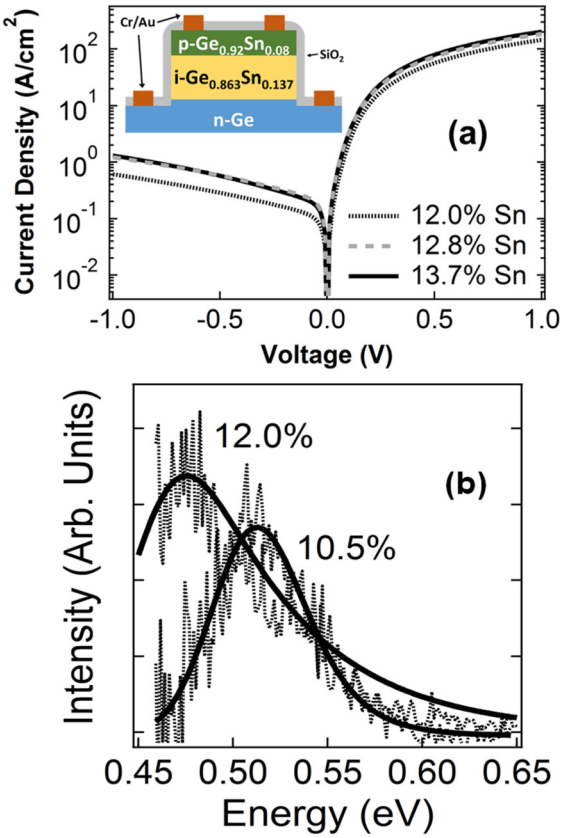

FIG. 4. (a) Schematic of a typical 13.7% Sn device. Dark current plots of the 13.7%, 12.8%, and 12.0% Sn devices are shown below. (b) EL plot of the 12% device is compared with that of a 10.5% analog described in prior work. The noise in the spectra is due to the thermoelectrically cooled PbS detector used in the experiment. The solid lines represent EMG fits to the data.

IV. GROWTH OF n-$Ge_{1-x}Sn_x$/i-$Ge_{1-y}Sn_y$/p-$Ge_{1-y}Sn_y$ DIODES

A possible limit to the strategy of using pure Ge buffer layers was encountered when attempting to grow alloys with Sn concentrations $y > 0.14$, for which the mismatch strain reaches 1.9%. This produced highly defected materials, making it difficult to fabricate devices with a performance comparable to the $y < 0.14$ counterparts. This issue was addressed by introducing an *n*-doped $Ge_{1-x}Sn_x$ intermediate layer between the active material and the Ge buffer to mitigate the starting lattice mismatch. The first example of this type of device was reported by Gallagher *et al.*, who produced diodes in which the three layers were $Ge_{1-y}Sn_y$ alloys with $y \approx 0.07$. These homo-structures yielded superior electroluminescence relative to hetero-structure *n*-Ge/*i*-$Ge_{1-y}Sn_y$/*p*-$Ge_{1-z}Sn_z$ analogs due to the absence of interface defects.[27]

In this study, *n*-$Ge_{1-x}Sn_x$/*i*-$Ge_{1-y}Sn_y$/*p*-$Ge_{1-y}Sn_y$ devices with $y = 0.15$–0.16 active layers were produced on Ge buffered Si. The samples utilized *n*-type $Ge_{1-x}Sn_x$ intermediate layers with Sn contents $x = 0.11$–0.12 which are lower than those of the active layer. Furthermore, the Sn content x was selected to be close enough to y to guarantee no strain relaxation at the *n*-*i* interface and at the same time limit the compressive strain in the active layers. Growth of the $Ge_{1-x}Sn_x$ layer was achieved using the SnD_4/Ge_3H_8 method described above for the 12% device. The $P(SiH_3)_3$ single source precursor was used to dope both the GeSn material and the Ge seed layer *n*-type with $9 \times 10^{18}\,cm^{-3}$ active carriers. The Si/Ge/$Ge_{1-x}Sn_x$ layers were removed from the growth chamber in order to measure the above composition and doping properties. Subsequently, the surface of the films was subjected to chemical cleaning using HF/H_2O solutions, and the samples were reinserted into the UHV-CVD chamber for the deposition of the active layers. These were grown at 260–265 °C using a Ge_3H_8/SnD_4 mixture with a Sn/Ge element ratio of 0.16. The *n*-*i*-*p* stacks were completed by *in-situ* doping the final 50–60 nm of the layer *p*-type using B_2H_6.

Figure 5 shows XRD reciprocal space maps of the 224 reflections for the *n*-Ge/$Ge_{0.89}Sn_{0.11}$/*i*-$Ge_{0.85}Sn_{0.15}$/*p*-$Ge_{0.85}Sn_{0.15}$ samples featuring an intrinsic $Ge_{0.85}Sn_{0.15}$ layer grown on a *n*-type $Ge_{0.89}Sn_{0.11}$ spacer and capped with a *p*-type $Ge_{0.85}Sn_{0.15}$ top electrode. The maps are well defined, narrow and symmetrical. Their vertical alignment indicates close lattice matching of the layers within the plane of growth, corroborating the notion that the relatively large lattice constant of $Ge_{0.89}Sn_{0.11}$ ($a = 5.7285$ Å) has allowed the active layer to grow pseudomorphically. An additional factor that may contribute to the pseudomorphic growth is the ultra-low temperatures of 260 °C utilized for the growth of these highly metastable alloy compositions. Furthermore, the XRD data suggest that the crystal quality of the $Ge_{0.85}Sn_{0.15}$ films is similar to that $Ge_{0.88}Sn_{0.12}$ analogs grown directly on virtual Ge substrates, as evidenced by comparable FWHM values of the (004) rocking curves of the two samples.

Complementary characterizations of strain and structure of the above 15% Sn devices were conducted by XTEM. A representative micrograph is shown in Figure 6(a), illustrating the entire device stack including the buffer layer, the *n*-*i*-*p* epilayers, and their respective interfaces. The data reveal that the

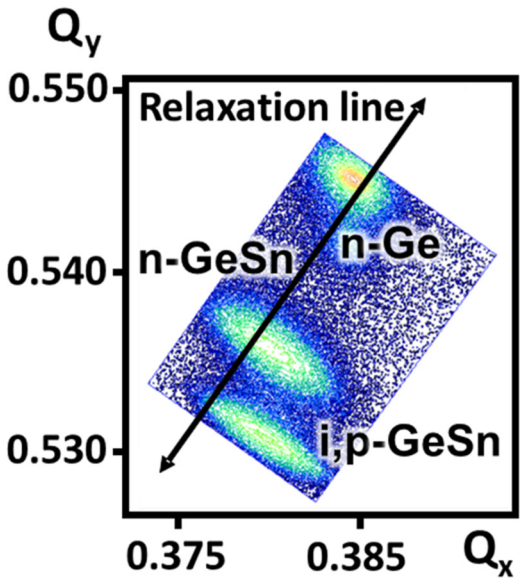

FIG. 5. HR-XRD reciprocal space maps of the *n*-$Ge_{0.89}Sn_{0.11}$/*i*-$Ge_{0.85}Sn_{0.15}$/*p*-$Ge_{0.85}Sn_{0.15}$ diode. The combined peaks of the *i* and *p* layers are vertically aligned with that of the *n*-layer indicating pseudomorphic growth. The *n* layer is 80% relaxed as indicated by the position of the 224 peak below the relaxation line.

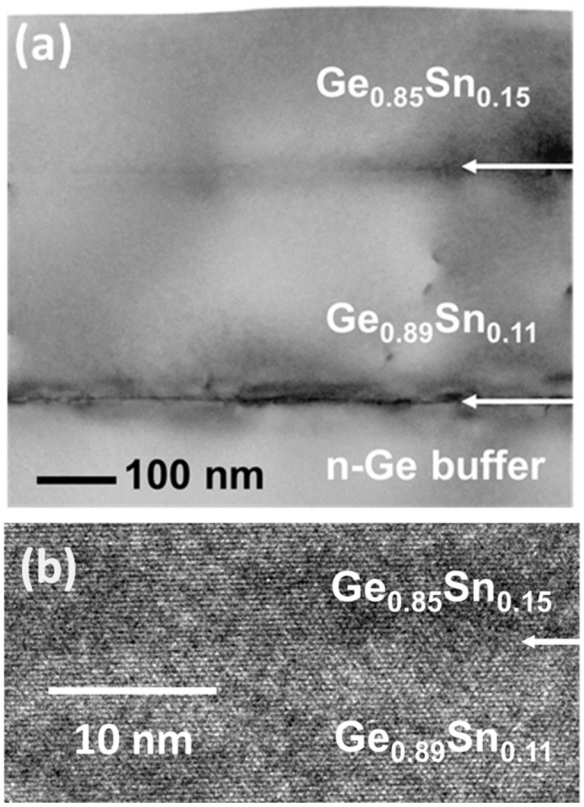

FIG. 6. XTEM micrographs of the n-Ge/n-$Ge_{0.89}Sn_{0.11}$/i-$Ge_{0.85}Sn_{0.15}$/p-$Ge_{0.85}Sn_{0.15}$ diode. (a) Diffraction contrast view of the entire device showing the various device layers and corresponding interfaces marked by arrows. (b) High resolution image of the bottom n-$Ge_{0.89}Sn_{0.11}$/i-$Ge_{0.85}Sn_{0.15}$ interface showing defect free pseudomorphic growth.

bulk crystal is largely devoid of threading dislocations in spite of the relatively high Sn content of 15%. The Ge/$Ge_{0.89}Sn_{0.11}$ bottom interface, marked by an arrow, is defective due to strain relaxation effects, while the upper n-$Ge_{0.89}Sn_{0.11}$/i-$Ge_{0.85}Sn_{0.15}$ analog is free of defects as evidenced by the uniform contrast in the vicinity of the top arrow. This is corroborated by high resolution images which show direct correspondence of the 111 lattice fringes between the two layers with no evidence of dislocations or other types of defects confined to the interface plane as illustrated in Figure 6(b). The top interface between the intrinsic and p-type $Ge_{0.85}Sn_{0.15}$ is not visible in the TEM images because of the flawless integration and continuous transition afforded by the homo-epitaxial character of the constituent layers (each containing the same 15% Sn). Finally, we note that XRD measurements of the n-Ge/n-$Ge_{0.88}Sn_{0.12}$/i-$Ge_{0.84}Sn_{0.16}$/p-$Ge_{0.63}Sn_{0.16}$ device revealed similar structural and strain properties as the 15% Sn analog, also indicating pseudomorphic growth of highly crystalline active and passive layers. This further confirms that the insertion of an intermediate layer between the active components and the Ge platform makes it possible to integrate ultrahigh Sn content materials with large thickness and suitable crystal quality to produce working diodes.

The I–V characteristics and schematic design of the fabricated diodes are shown in Figure 7. In both cases, the bottom contacts were made to the n-Ge layer, while the top contacts were deposited on the p- layer as indicated in Figure 7(a). Figure 7(b) shows that the reverse bias currents are

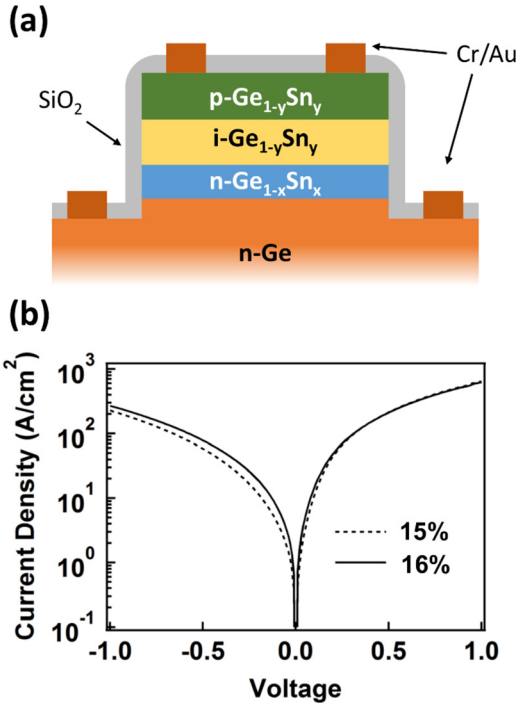

FIG. 7. (a) Schematic representations of n-Ge/n-$Ge_{1-x}Sn_x$/i-$Ge_{1-y}Sn_y$/p-$Ge_{1-y}Sn_y$ diode structure in which the bottom contacts are made to the n-Ge layer. (b) I-V curves obtained from devices with above diode design consisting of $y = 0.15$–0.16 active layers.

significantly higher than previously observed for the 12%–13.7% analogs, as depicted in Figure 4. This might indicate a significant degradation of the material's quality past the $y = 14\%$ limit, but the TEM data in Figure 6 and a closer examination of the electrical results suggest otherwise. In Figure 8, we compare the reverse-bias currents of devices grown on pure Ge and $Ge_{1-x}Sn_x$ buffer layers depicted as Ge/$Ge_{1-y}Sn_y$/$Ge_{1-z}Sn_z$ and $Ge_{1-x}Sn_x$/$Ge_{1-y}Sn_y$/$Ge_{1-z}Sn_z$, respectively. We see a drastic increase by almost two orders of magnitude in the samples grown on $Ge_{1-x}Sn_x$ buffers, even though in this case the interface with the intrinsic layer in most cases is pseudomorphic and defect free (see Figure 6), whereas in the pure Ge case it is relaxed and highly defected. While the higher reverse bias currents could be due

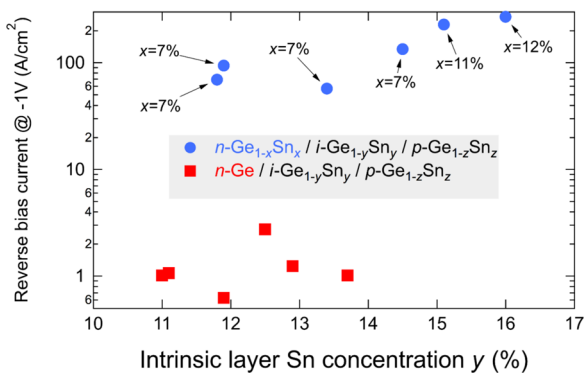

FIG. 8. Comparison of diode currents at −1 V bias between Ge/GeSn/GeSn (red squares) and GeSn/GeSn/GeSn (blue circles) diodes. Note the dramatic increase in reverse bias currents as the n-layer approaches direct gap conditions, even though the n-i interface is less defected. The higher currents are assigned to band-to-band tunneling.

to an increase in point defects as the Sn concentration is increased, rather than to extended defects associated with strain relaxation, we note that for the *same* intrinsic layer Sn concentrations y, the reverse bias currents are drastically higher when the n-type layer consists of a $Ge_{1-x}Sn_x$ alloy. This suggests that point defects in the intrinsic layer are not responsible for the higher reverse-bias current. Furthermore, for the higher values of y the corresponding value of x is about 11%, but when $Ge_{0.89}Sn_{0.11}$ is used as an intrinsic layer in devices grown on pure Ge, the reverse-bias currents are low. In other words, there is no device evidence for a higher density of point defects associated with the Sn concentration in any of the device components. We believe that the explanation for the higher reverse bias currents is band-to-band-tunneling, which, as reported by Schulte-Braucks *et al.*,[30] is drastically enhanced when the n-type layer is a direct gap material. The key difference between the diodes in Fig. 7 and those in Fig. 4 is that the in the case of Fig. 4 the n-type layer is pure Ge, which is indirect, but in the case of Fig. 7 it is $Ge_{0.89}Sn_{0.11}$, which is a direct-gap alloy. This explains the dramatically increased tunneling current.

V. DISCUSSION

We have demonstrated that the Ge_3H_8/SnD_4 route makes it possible to synthesize $Ge_{1-y}Sn_y$ alloys with Sn concentrations as high as $y = 16\%$ that can be incorporated into working devices. We find that at high Sn-concentrations the main factor limiting the amount of Sn that can be incorporated—while maintaining the device integrity—is the same found at lower Sn-concentrations, namely, the mismatch strain between the $Ge_{1-y}Sn_y$ layer and the underlying buffer layer. Provided that this mismatch strain is kept moderately low, we find that good quality films can be obtained with Sn concentrations as high as 16%. This suggests that even higher Sn concentrations may be attainable by this method by growing successive layers of ever increasing Sn concentrations, following a process similar to the early efforts to grow Ge on Si by using intermediate $Ge_{1-x}Si_x$ layers of graded composition.[31] The ultimate limit of this approach may be given by the ever decreasing growth temperature needed to incorporate an increasing amount of Sn.

From an optical perspective, a disadvantage of the "graded" layer approach is that the intrinsic layer with a higher Sn concentration is under compressive strain, which makes the semiconductor less direct. Figure 9(a) shows a band diagram for a $Ge_{0.89}Sn_{0.11}/Ge_{0.84}Sn_{0.16}$ heterostructure in which we see that the strained $Ge_{0.84}Sn_{0.16}$ alloy is direct by only 33 meV. In addition, the structure is type-II, which is unsuitable for light emission. A possible solution to this problem would be to grade the buffer layer to match the intrinsic layer Sn-concentration, so that the intrinsic layer is relaxed and the n/p layers are under tensile strain. The corresponding band lineup is shown in Fig. 9(b), and we see that band gap "directness" has markedly improved to 81 meV. However, the heterostructure remains type II. A possible way to achieve a type-I alignment is to add Si to the barrier layer, as shown in Figure 9(c). However, this increases the strain in this layer, suggesting that the desired type-I alignment may require very thin layers to avoid strain relaxation.

While the calculations in Fig. 9 provide some guidance for future advances, it is important to stress that they depend on some very poorly known parameters, such as the band offsets in the Si-Ge-Sn system and the compositional dependence of the band gaps in the ternary $Ge_{1-x-y}Si_xSn_y$ alloys. In addition, several deformation potentials are needed for the alloy system, and these are usually taken as linear interpolations between experimental or theoretical values for the elemental semiconductors. The general scheme for our calculations was given in Ref. 32. We took the compositional dependence of the direct and indirect edges in $Ge_{1-y}Sn_y$ alloys from Ref. 9, and for the ternary $Ge_{1-x-y}Si_xSn_y$ we also used a quadratic polynomial with a bowing parameter $b^{SiSn} = 14$ eV.[33] For the deformation potentials, we used the values recommended in Refs. 29 and 34. The band offsets depend on the relative alignment of the average valence band value $E_{v,av}$, as defined by Van de Walle.[35] In Refs. 36 and 32, and in many subsequent papers modeling heterostructures containing $Ge_{1-y}Sn_y$ and $Ge_{1-x-y}Si_xSn_y$ layers, the relative alignment of $E_{v,av}$ for Si, Ge, and α-Sn was taken from a simplified theory of band offsets by Jaros.[37] This was done due to the dearth of theoretical and experimental data for α-Sn. More recently,

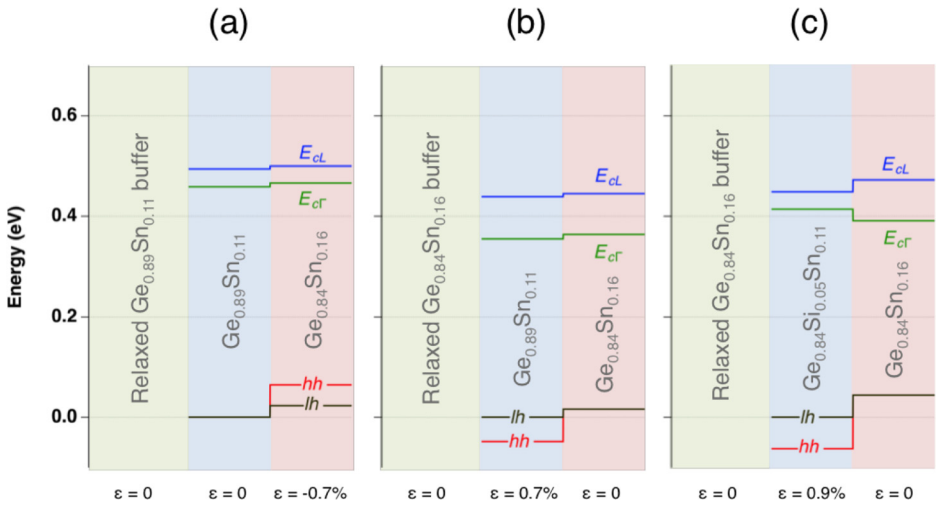

FIG. 9. Calculated band lineup at different GeSn/GeSiSn pseudomorphically strained heterostructures. E_{cL}: conduction band minimum at the L-point of the BZ. $E_{c\Gamma}$: conduction band minimum at the Γ-point of the BZ. hh (lh): heavy (light) hole band at the Γ-point of the BZ. The strain is indicated below each of the layers.

however, Li *et al.*[38] published new *ab initio* calculations of band offsets that imply $E_{v,\mathrm{av}}$ values quite different from those previously calculated. If we conventionally assume $E_{v,\mathrm{av}}(\mathrm{Ge}) = 0$, Li *et al.* predict $E_{v,\mathrm{av}}(\mathrm{Si}) = -0.755\,\mathrm{eV}$ for Si, substantially larger than the value $E_{v,\mathrm{av}}(\mathrm{Si}) = -0.48\,\mathrm{eV}$ from Jaros' theory, and also higher than Van de Walle's values $E_{v,\mathrm{av}}(\mathrm{Si}) = -0.53\,\mathrm{eV}$ (Ref. 39) and $E_{v,\mathrm{av}}(\mathrm{Si}) = -0.68\,\mathrm{eV}$ (Ref. 35). Interestingly, recent work has shown that the type-II band alignment at a $Si_{0.70}Ge_{0.30}$/Si heterostructure, as obtained by Thewalt *et al.* from photoluminescence measurements,[40] imply $E_{v,\mathrm{av}}(\mathrm{Si}) = -0.800\,\mathrm{eV}$, and subsequent capacitance-voltage measurements at Si/$Ge_{1-x}Si_x$ interfaces are also in very good agreement with this value.[34] These results provide strong support for Li's theoretical results. Accordingly, we use for a $Ge_{1-x-y}Si_xSn_y$ alloy

$$E_{v,\mathrm{av}}(x,y) = 3(1-x-y)a_v^{\mathrm{Ge}}\frac{[a_0(x,y)-a_0^{\mathrm{Ge}}]}{a_0^{\mathrm{Ge}}} + x\left\{E_{v,\mathrm{av}}(\mathrm{Si}) + 3a_v^{\mathrm{Si}}\frac{[a_0(x,y)-a_0^{\mathrm{Si}}]}{a_0^{\mathrm{Si}}}\right\} + y\left\{E_{v,\mathrm{av}}(\mathrm{Sn}) + 3a_v^{\mathrm{Sn}}\frac{[a_0(x,y)-a_0^{\mathrm{Sn}}]}{a_0^{\mathrm{Sn}}}\right\}, \quad (4)$$

where $E_{v,\mathrm{av}}(\mathrm{Si}) = -0.800\,\mathrm{eV}$ and $E_{v,\mathrm{av}}(\mathrm{Sn}) = 0.904\,\mathrm{eV}$. The latter is obtained from the Li value $E_{v,\mathrm{av}}(\mathrm{Sn}) = 0.852\,\mathrm{eV}$ after renormalizing by the same factor (0.800/0.755) that in the Ge-Si system brings theory into exact agreement with experiment. Eq. (4) implies that $E_{v,\mathrm{av}}$ for the alloy is computed as a linear interpolation of the $E_{v,\mathrm{av}}$'s for Si, Ge, and α-Sn, corrected for their hydrostatic shift to account for the difference between the cubic lattice parameter $a_0(x,y)$ of the alloy and the cubic lattice parameters $a_0^{\mathrm{Si}}, a_0^{\mathrm{Ge}}, a_0^{\mathrm{Sn}}$ of the elemental semiconductors. The correction terms contain the absolute valence band hydrostatic deformation potentials for Si (a_v^{Si}), Ge (a_v^{Ge}), and α-Sn (a_v^{Sn}). We use $a_v^{\mathrm{Si}} = 2.24\,\mathrm{eV}$, $a_v^{\mathrm{Ge}} = 2.10\,\mathrm{eV}$, and $a_v^{\mathrm{Sn}} = 1.49\,\mathrm{eV}$. These values were obtained by multiplying the *ab initio* predictions of Li *et al.* (Ref. 41) times 0.94, so that the band gap deformation potential in Ge is matched exactly. The procedure is described in Ref. 34. Recently, Yamaha *et al.* published band offset measurements at Ge/$Ge_{1-x-y}Si_xSn_y$ interfaces.[42] For a Ge/$Ge_{0.44}Si_{0.41}Sn_{0.15}$ alloy, the valence band offset was found to be 0.11 eV (higher on the Ge side), which should be compared with 0.15 eV predicted in a calculation of the heterostructure using Eq. (4) for $E_{v,\mathrm{av}}(x,y)$. Moreover, if we reduce the Si concentration to 39% in order to match the measured strain exactly, we predict a valence band offset of 0.13 eV, in even better agreement with the measurements in Ref. 42. This level of agreement can be considered very satisfactory given the sensitivity to the compositions and the fact that the band offsets were extracted by approximating the valence band density of states as a linear function of energy near the band edge, rather than by trying to model it using realistic expressions. Nevertheless, it is apparent that further work is needed to determine the validity of Eq. (4) as well as the compositional dependence of band gaps in the $Ge_{1-x-y}Si_xSn_y$ layers, which affects strongly the range of type-I structures that can be obtained.

VI. SUMMARY

We have developed CVD reactions that have enabled the fabrication of thick, highly concentrated $Ge_{1-y}Sn_y$ layers (y = 0.12%–0.16%) possessing tunable band gaps within the desirable long wave mid IR range. These materials are grown on Ge buffered Si wafers and in turn used to fabricate working *p-i-n* diodes whose optical and electrical properties are investigated by electroluminescence and I-V measurements. For devices with 12–14% Sn contents, the active layers are grown directly on the Ge buffer and capped with a $Ge_{1-z}Sn_z$ top electrode thus producing a partially lattice matched stack of the form *n*-Ge/*i*-$Ge_{1-y}Sn_y$/*p*-$Ge_{1-z}Sn_z$ containing a single defected bottom interface. For 15%–16% Sn devices, an intermediate $Ge_{1-x}Sn_x$ layer is needed to overcome the ever increasing strain mismatch of the active material and the Ge buffer. This creates lattice-matched hetero-structures of the form *n*-$Ge_{1-x}Sn_x$/*i*-$Ge_{1-y}Sn_y$/*p*-$Ge_{1-z}Sn_z$ featuring slightly compressive and fully coherent active materials that are devoid of extended defects induced by strain relaxation. In spite of the excellent crystal quality observed by XTEM, the dark currents of the latter devices are two orders of magnitude higher than the former. This behavior is explained by a band-to-band-tunneling mechanism that is further enhanced when the *n*- bottom layer is a direct gap material as in the case of the *n*-$Ge_{1-x}Sn_x$/*i*-$Ge_{1-y}Sn_y$/*p*-$Ge_{1-z}Sn_z$ prototype. In light of this observation, we propose various device alternatives that promote the formation of type I designs for applications in future generation lasers and LEDs operating in the mid IR.

ACKNOWLEDGMENTS

This work was supported by the U.S. Air Force under Contract Nos. AFOSR FA9550-12-1-0208 and AFOSR FA9550-13-1-0022. We gratefully acknowledge the use of the John M. Cowley Center for High Resolution Electron Microscopy and the Ira A. Fulton Center for Solid State Electronics Research at Arizona State University.

[1]M. Bauer, J. Taraci, J. Tolle, A. V. G. Chizmeshya, S. Zollner, D. J. Smith, J. Menendez, C. Hu, and J. Kouvetakis, Appl. Phys. Lett. **81**, 2992 (2002).
[2]J. P. Fleurial, J. Electrochem. Soc. **137**, 2928 (1990).
[3]F. L. Freitas, J. Furthmüller, F. Bechstedt, M. Marques, and L. K. Teles, Appl. Phys. Lett. **108**, 092101 (2016).
[4]H. H. Tseng, K. Y. Wu, H. Li, V. Mashanov, H. H. Cheng, G. Sun, and R. A. Soref, Appl. Phys. Lett. **102**, 182106 (2013).
[5]W. Du, Y. Zhou, S. A. Ghetmiri, A. Mosleh, B. R. Conley, A. Nazzal, R. A. Soref, G. Sun, J. Tolle, J. Margetis, H. A. Naseem, and S.-Q. Yu, Appl. Phys. Lett. **104**, 241110 (2014).
[6]S. Wirths, D. Buca, and S. Mantl, Prog. Cryst. Growth Charact. Mater. **62**, 1 (2016).
[7]S. Wirths, R. Geiger, N. von den Driesch, G. Mussler, T. Stoica, S. Mantl, Z. Ikonic, M. Luysberg, S. Chiussi, J. M. Hartmann, H. Sigg, J. Faist, D. Buca, and D. Grützmacher, Nat. Photonics **9**, 88 (2015).
[8]J. D. Gallagher, C. L. Senaratne, P. Sims, T. Aoki, J. Menéndez, and J. Kouvetakis, Appl. Phys. Lett. **106**, 091103 (2015).
[9]J. D. Gallagher, C. L. Senaratne, J. Kouvetakis, and J. Menéndez, Appl. Phys. Lett. **105**, 142102 (2014).
[10]G. Sun, R. A. Soref, and H. H. Cheng, J. Appl. Phys. **108**, 033107 (2010).
[11]S. J. Sweeney, A. R. Adams, M. Silver, E. P. O'Reilly, J. R. Watling, A. B. Walker, and P. J. A. Thijs, Phys. Status Solidi **211**, 525 (1999).
[12]C. I. Ventura, J. D. Fuhr, and R. A. Barrio, Phys. Rev. B **79**, 155202 (2009).

[13]F. Gencarelli, B. Vincent, L. Souriau, O. Richard, W. Vandervorst, R. Loo, M. Caymax, and M. Heyns, Thin Solid Films **520**, 3211 (2012).
[14]E. Woelk and R. Loo, Solid State Technol. **58**, 37 (2014).
[15]G. Grzybowski, R. T. Beeler, L. Jiang, D. J. Smith, J. Kouvetakis, and J. Menéndez, Appl. Phys. Lett. **101**, 072105 (2012).
[16]R. F. Spohn and C. B. Richenberg, ECS Trans. **50**, 921 (2013).
[17]E. Rivard, Chem. Soc. Rev. **45**, 989 (2016).
[18]N. von den Driesch, D. Stange, S. Wirths, G. Mussler, B. Holländer, Z. Ikonic, J. M. Hartmann, T. Stoica, S. Mantl, D. Grützmacher, and D. Buca, Chem. Mater. **27**, 4693 (2015).
[19]J. E. Bentham, S. Cradock, and E. A. V. Ebsworth, Inorg. Nucl. Chem. Lett. **7**, 1077 (1971).
[20]A. Feltrin and A. Freundlich, Renewable Energy **33**, 180 (2008).
[21]C. L. Senaratne, J. D. Gallagher, L. Jiang, T. Aoki, J. Menéndez, and J. Kouvetakis, J. Appl. Phys. **116**, 133509 (2014).
[22]M. Oehme, J. Werner, M. Gollhofer, M. Schmid, M. Kaschel, E. Kasper, and J. Schulze, IEEE Photonics Technol. Lett. **23**, 1751 (2011).
[23]M. Oehme, E. Kasper, and J. Schulze, ECS J. Solid State Sci. Technol. **2**, R76 (2013).
[24]M. Oehme, K. Kostecki, T. Arguirov, G. Mussler, K. Ye, M. Gollhofer, M. Schmid, M. Kaschel, R. A. Korner, M. Kittler, D. Buca, E. Kasper, and J. Schulze, IEEE Photonics Technol. Lett. **26**, 187 (2014).
[25]E. Kasper and M. Oehme, Jpn. J. Appl. Phys., Part 1 **54**, 04DG11 (2015).
[26]C. Xu, J. D. Gallagher, P. Sims, D. J. Smith, J. Menéndez, and J. Kouvetakis, Semicond. Sci. Technol. **30**, 045007 (2015).
[27]J. D. Gallagher, C. L. Senaratne, C. Xu, P. Sims, T. Aoki, D. J. Smith, J. Menéndez, and J. Kouvetakis, J. Appl. Phys. **117**, 245704 (2015).
[28]R. Beeler, R. Roucka, A. V. G. Chizmeshya, J. Kouvetakis, and J. Menéndez, Phys. Rev. B **84**, 035204 (2011).
[29]L. Jiang, J. D. Gallagher, C. L. Senaratne, T. Aoki, J. Mathews, J. Kouvetakis, and J. Menéndez, Semicond. Sci. Technol. **29**, 115028 (2014).
[30]C. Schulte-Braucks, D. Stange, N. von den Driesch, S. Blaeser, Z. Ikonic, J. M. Hartmann, S. Mantl, and D. Buca, Appl. Phys. Lett. **107**, 042101 (2015).
[31]S. B. Samavedam, M. T. Currie, T. A. Langdo, and E. A. Fitzgerald, Appl. Phys. Lett. **73**, 2125 (1998).
[32]V. R. D'Costa, Y.-Y. Fang, J. Tolle, J. Kouvetakis, and J. Menéndez, Thin Solid Films **518**, 2531 (2010).
[33]V. R. D'Costa, Y.-Y. Fang, J. Tolle, J. Kouvetakis, and J. Menéndez, Phys. Rev. Lett. **102**, 107403 (2009).
[34]J. T. Teherani, W. Chern, D. A. Antoniadis, J. L. Hoyt, L. Ruiz, C. D. Poweleit, and J. Menéndez, Phys. Rev. B **85**, 205308 (2012).
[35]C. G. Van de Walle, Phys. Rev. B **39**, 1871 (1989).
[36]J. Menéndez and J. Kouvetakis, Appl. Phys. Lett. **85**, 1175 (2004).
[37]M. Jaros, Phys. Rev. B **37**, 7112 (1988).
[38]Y. H. Li, A. Walsh, S. Chen, W. J. Yin, J. H. Yang, J. Li, J. L. F. Da Silva, X. G. Gong, and S. H. Wei, Appl. Phys. Lett. **94**, 212109 (2009).
[39]C. G. Van De Walle and R. M. Martin, Phys. Rev. B **34**, 5621 (1986).
[40]M. L. W. Thewalt, D. A. Harrison, C. F. Reinhart, and J. A. Wolk, Phys. Rev. Lett. **79**, 269 (1997).
[41]Y.-H. Li, X. G. Gong, and S.-H. Wei, Phys. Rev. B **73**, 245206 (2006).
[42]T. Yamaha, S. Shibayama, T. Asano, K. Kato, M. Sakashita, W. Takeuchi, O. Nakatsuka, and S. Zaima, Appl. Phys. Lett. **108**, 061909 (2016).